Journal of Ceramic Processing Research. Vol. 24, No. 2, pp. 216~221 (2023)
(Received 6 July 2022, Received in revised form 29 September 2022, Accepted 3 November 2022)
https://doi.org/10.36410/jcpr.2023.24.2.216

J O U R N A L O F
Ceramic Processing Research

Comparative study of WC-Co-VC-Cr_3C_2 cemented carbide by spark plasma sintering: densification, microstructure, and mechanical properties

Jeong-Han Lee, Jae-Cheol Park, Bum-Soon Park and Hyun-Kuk Park*
Automotive Materials & Component R&D Group, Korea Institute of Industrial Technology, Gwangju 61012, Korea

Ultrafine-grained WC-Co-VC-Cr_3C_2 cemented carbide was consolidated from homogeneously synthesized powder using spark plasma sintering at 1300 °C under 60 MPa. The densification behavior of WC-Co-VC-Cr_3C_2 was determined based on the shrinkage strain with sintering kinetics. As the Cr_3C_2 addition increased, the secondary (Cr, W)C_x phase was attributed to abnormal grain growth in the basal facet of WC, whereas grain boundary strengthening was induced by the separation of the WC/Co interface with the addition of VC. The mechanical properties of WC-Co-VC-Cr_3C_2 cemented carbide depend on the grain size and lattice strain of the hard phase, in contrast to the toughening mechanism, and were correlated with the crack propagation and fracture resistance. The WC-Co-Cr_3C_2 cemented carbide with the best combination of mechanical properties was found, including a hardness of 1958.9 kg/mm^2 and fracture toughness of 7.3 MPa·m$^{1/2}$.

Keywords: Cemented carbide, transition metal carbide, sintering kinetics, spark plasma sintering, mechanical property.

Introduction

WC-Co cemented carbide has a high melting point, strength, and corrosion/heat resistance; therefore, it is used in various applications such as in wear resistant parts, cutting tools for metallic/ceramic materials, and molds [1-3]. The mechanical properties of WC-Co cemented carbide depend on the porosity, particle size, and binder content of the carbide. In particular, it is important to control the grain growth of the carbide during consolidation (diffusion or sintering) [4].

Recently, a small amount of a transition metal carbide (TMC) such as TaC, VC, NbC, TiC, Mo_2C, or Cr_3C_2 has been added to improve the hardness through the grain refinement of the carbide or to improve the interfacial stability through the formation of a secondary phase such as (W, TM)C to enhance the fracture toughness and transverse rupture strength [5-8]. However, the mechanical properties may deteriorate because of the formation of a concentrated secondary phase against free carbon precipitation or the W_2C phase as a result of a difference in carbon activity in carbide with certain content [9]. Therefore, this implies that the coherency of the interface at each carbide could be used as an important factor in designing WC-Co-TMC cemented carbide. Because VC has the lowest complexion forming energy of the various (W, TM)C examples, a stable interface can be maintained under a high-energy interface, resulting in a highly coherent interface, along with the WC grain refinement effect, *e.g.*, (W, Cr)C_x: 2.778 eV, (W, Ta)C_x:2.426 eV, WC_x:2.167 eV, (W, V)C_x:1.576 eV, and (W, Nb)C_x:1.481 eV [10].

According to previous studies [11-13], spark plasma sintering (SPS) is an effective consolidation method for cemented carbide, wherein adding a grain growth inhibitor (GGI) can lead to grain boundary (G/B) strengthening by controlling the refined grain size in the carbide (WC) at the submicrometer level. For example, VC and Cr_3C_2 are effective mediators that result in hardened G/Bs owing to the high solubility of the binder interfaces [6].

In this study, an alloy composition was designed to closely examine the effect of the addition of Cr_3C_2 on WC-Co-VC-based cemented carbides. WC, Co, VC, and Cr_3C_2 raw materials were homogeneously synthesized via a horizontal ball-milling process. The SPS process was performed at a high density during solid-state consolidation throughout the hardened phase against the binder and secondary phases. The structural and microstructural evolution, densification behavior, and mechanical properties of the WC-Co-VC-Cr_3C_2 cemented carbides were investigated based on the sintering kinetics, grain size, lattice strain, and trace of crack microstructures.

Experimental

WC (≤0.5 μm, >99.9%, Taegutec Ltd.), Co (≤10.0 μm, >99.8%, Alfa Aesar), VC (≤2.0 μm, >99.5%, Alfa Aesar), and Cr_3C_2 (≤10.0 μm, >99.5%, Alfa Aesar) powders were used as raw materials. The ball-milling process was performed using a horizontal type mill

*Corresponding author:
Tel : +82-62-600-6270
Fax: +82-62-600-6149
E-mail: hk-park@kitech.re.kr

with ZrO_2 balls at a ball-to-powder ratio of 10:1. The powder mixture was synthesized for 24 h in ethanol at 300 rpm. The nominal compositions were classified as WC-6Co-2.5VC-(0.5, 1.0, 1.5, and 2.0)-Cr_3C_2. The phase and lattice structures of the WC-Co-VC-Cr_3C_2 cemented carbides were investigated using X-ray diffraction (XRD, PIXCEL 1D DETECTOR, Panalytical) with CuKα radiation (λ = 0.154 nm). The average crystallite size and microstrain were analyzed using the Williamson Hall (W-H) method, as shown in Eq. (1) [14]:

$$D = \frac{k\lambda}{\beta_{hkl}\cos\theta},\ \varepsilon = \frac{\beta_{hkl}}{4\tan\theta}, \tag{1}$$

Where D is the crystallite size, k is the Scherrer constant (0.9) with the shape factor, and λ is the wavelength of the CuKα radiation. Instrumental broadening is expressed as the β_{hkl} of the corrected value derived using the microstrain (ε). In addition, the WC grain size was determined from field emission scanning electron miscroscopy (FE-SEM) images using Image-Pro software (6.0 ver., Media Cybernetics) to measure the linear intercept length. The microstructure of the WC-Co-VC-Cr_3C_2 cemented carbides was investigated using FE-SEM (JSM-7001F, JEOL).

The dislocation density was measured using the Williamson–Smallman approach [15], as shown in Eq. (2), where the crystallite size and microstrain determine the following reaction:

$$\rho = (\rho_D\rho_S)^{\frac{1}{2}},\ \left(\rho_D = \frac{3}{D^2},\ \rho_S = \frac{k\varepsilon^2}{b^2}\right), \tag{2}$$

Where ρ is the dislocation density, ρ_D is the crystallite constant, ρ_S is the strain constant, and b is the dislocation Burgers vector.

The mechanical properties (hardness and fracture toughness) were measured using a Vickers hardness tester (HM-100, Mitutoyo) with an applied load of 20 kgf for 15 s. The hardness was calculated using Eq. (3):

$$H_v = \frac{kP}{d^2}, \tag{3}$$

Where k is a constant (=1.89 × 10^5) that depends on the indenter geometry and units, P is the applied force (in N), and d is the diagonal length of the indentation. In addition, the fracture toughness (K_{IC}) obtained using the Antis formula [16] was expressed using Eq. (4).

$$K_{IC} = 0.016\left(\frac{E}{Hv}\right)^{1/2} P/C^{3/2} \tag{4}$$

Results and Discussion

Figure 1 shows the phase constituents of the WC-Co-VC-Cr_3C_2 cermets from the evolution of the powder to the sintered compacts. The phase combinations of the sintered compacts included WC, Co, and (W, TM)C_x, and there was a clear difference in the peak intensity related to the grain growth direction of the cemented carbide, *i.e.*, (001) basal and (100) prismatic facets. The intensity ratio (I_r), expressed as [$(001)_{basal}/(001)_{prismatic}$ = I_r], was calculated from the integral diffraction data according to the co-addition of VC and Cr_3C_2 and could be correlated with the grain growth and mechanical properties [17], *i.e.*, WC-6Co (#1):0.39, WC-6Co-2.5VC (#2):0.38, WC-6Co-2.5VC-0.5Cr_3C_2 (#3):0.40, WC-6Co-2.5VC-1.0Cr_3C_2 (#4):0.41, WC-6Co-2.5VC-1.5Cr_3C_2 (#5):0.45, and WC-6Co-2.5VC-2.0Cr_3C_2 (#6):0.59. An increase in I_r was attributed to the preferentially oriented growth of WC grains, accompanied by a lack of interfacial stability, such as the misfit of phase boundaries. This was because a

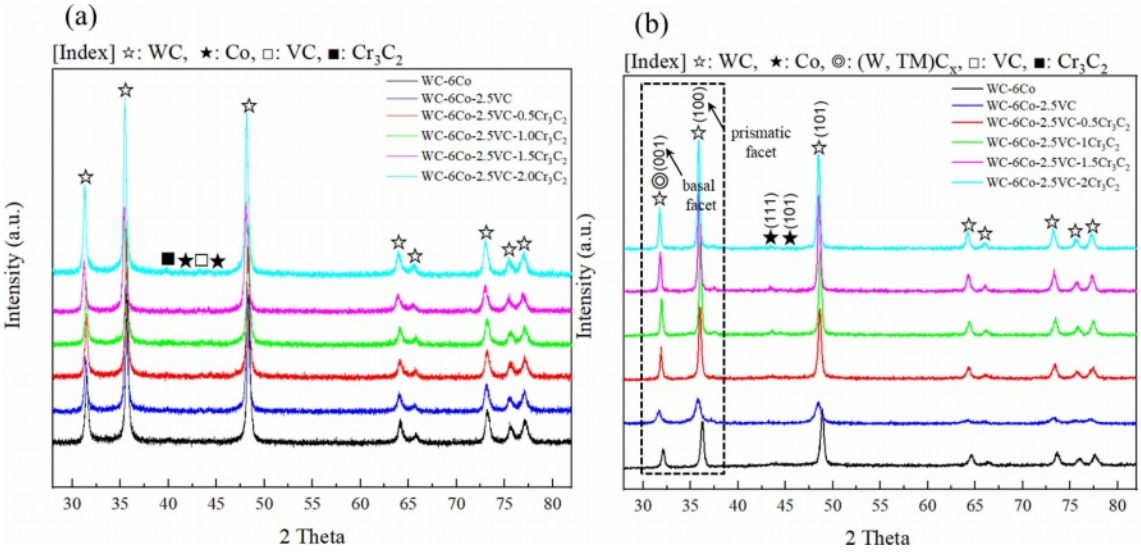

Fig. 1. XRD patterns of the WC-Co-VC-Cr_3C_2 cermet: (a) milled-powder and (b) sintered-compacts.

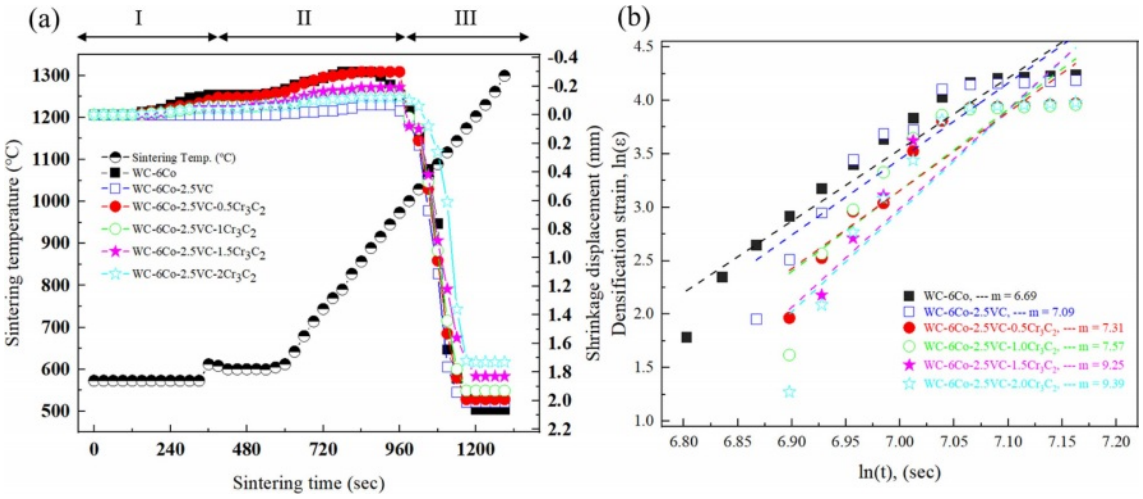

Fig. 2. Sintering behavior of the WC-Co-VC-Cr_3C_2 cermet: (a) shrinkage displacement with sintering time and temperature profile, and (b) densification strain-sintering time curve in shrinkage stage, i. e., at the temperature range of (900~1300) °C.

decrease in the total interfacial energy can act as a driving force for grain growth, and it is believed that the addition of a higher Cr_3C_2 concentration (>1.5 wt%) causes preferential growth in the basal facet with relatively low energy at the WC interface, *i.e.*, basal: 1.07-1.34 $J \cdot m^{-2}$ and prismatic: 1.43-3.02 $J \cdot m^{-2}$ [18].

Figure 2 shows the densification profiles and sintering kinetics of the WC-Co-VC-Cr_3C_2 cermets. The relative densities of all the samples were found to be above 95.0% using the Archimedes method (#1, 100.0%; #2, 99.2%; #3, 98.3%; #4, 98.1%; #5, 96.6%; and #6, 95.8%). The shrinkage behavior (*see* Fig. 2a) depended on the binder content. Rapid sintering could be divided into three main sections (I-III). In the early section (I) (~600 °C), infrared pyrometer detection showed that only 2-3% densification with slight shrinkage from particle-particle contact was achieved from the starting green body, whereas the intermediate section (II) (600-

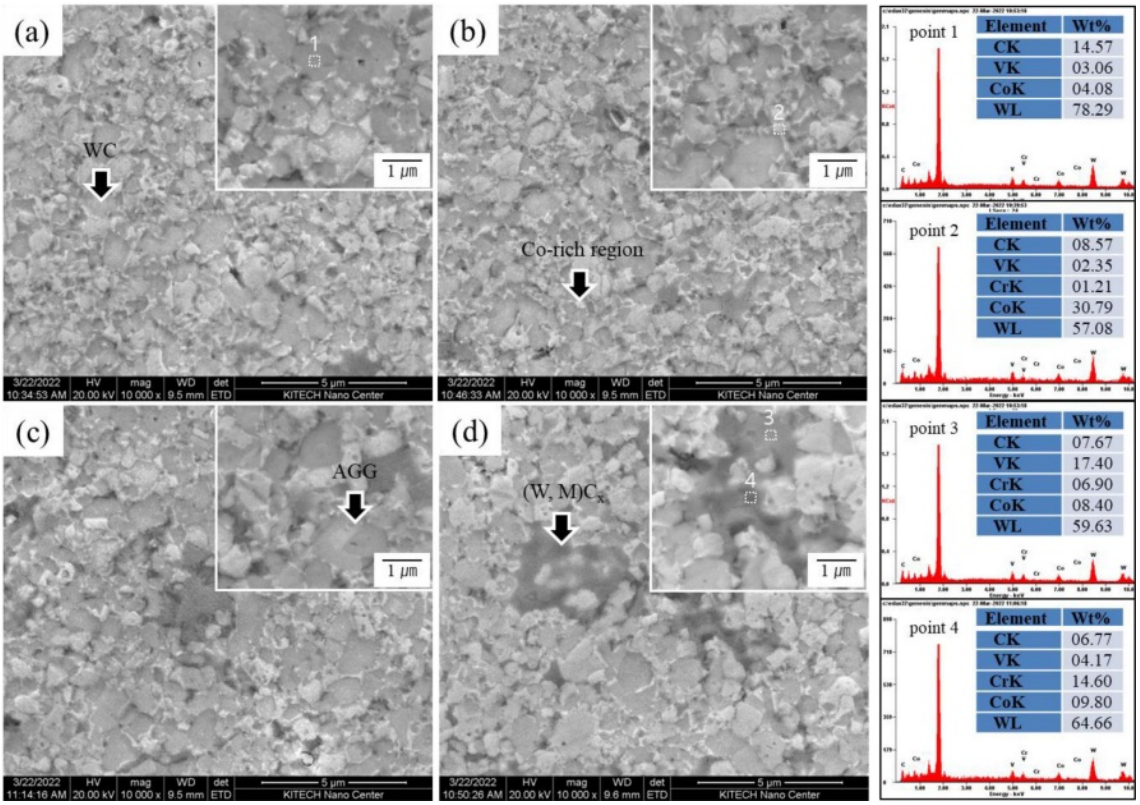

Fig. 3. Microstructures and quantitative analysis of the WC-Co-VC-Cr_3C_2 cermet sintered at 1300°C: (a) WC-6Co-2.5VC-0.5Cr_3C_2, (b) WC-6Co-2.5VC-1.0Cr_3C_2, (c) WC-6Co-2.5VC-1.5Cr_3C_2, and (d) WC-6Co-2.5VC-2.0Cr_3C_2.

900 °C) showed rapid shrinkage from active diffusion, including mass transport, surface diffusion, grain boundary migration, and volume diffusion. The final densification (III) (900-1300 °C) consolidated the removal of closed pores, corresponding to the saturation of the shrinkage behavior. The sintering exponent (m) and densification strain (ε) in the final stage are shown in Fig. 2b. With a larger sintering index, the shorter shrinkage displacement was related to the active diffusion path for densification from the interface energetics and transport kinetics [19]. Therefore, WC-6Co with the lowest "m" value (6.69) showed the highest densification strain, which was believed to be due to the highly active diffusion routes at the lattice and grain boundaries throughout section III.

Figure 3 shows the microstructures of the sintered WC-Co-VC-Cr_3C_2 cermets. They consisted of angular WC grains and Co-binder (bright grey) between the WC grain boundaries, with the (M, W)C_x phase (dark grey) locally embedded in the WC grains. When more than a certain amount of Cr_3C_2 (>1.5 wt%) was added, an abnormal grain growth (AGG) was observed, which was due to the high solubility of Cr in Co during the recrystallization process of WC. This was because hardly any interfacial segregation occurred, with continuous grain growth according to the rearrangement of WC grains rather than hindered grain growth by complexions under a high interfacial energy with the addition of VC [20]. Peng et al. calculated the thermodynamic solubility of Cr and V in a Co binder, *i.e.*, Cr:6.2 to 11.4 wt% and V: 1.1-2.2 wt% [21]. In other words, the concentrated Cr_3C_2 was mostly dissolved in the WC/Co interface. Thus, it could not properly perform the role of a GGI, as expected from a conventional TMC addition. Consequently, it was believed that the coarsened WC grains in the final sintering step caused nucleation in the basal facet rather than recrystallization by grain boundary migration.

The above-mentioned details of the structural evolution were scrutinized during the measurements of the crystallite (by XRD) and grain size (by FE-SEM) of the WC, along with the dislocation density (by XRD), as shown in Fig. 4. With the co-addition of VC and Cr_3C_2, the grain size of WC increased from 0.71 to 0.92 μm, and the crystallite size also increased from 38.9 to 50.2 nm. However, it was found that the single addition of VC caused grain refinement by the GGI effect, which corresponded to an increase in the dislocation density (ρ) from 3.41 to 6.70×10^{15} m^{-2}. The grain refinement was attributed to an increase in the dislocation density with an increase in the interfacial energy. Owing to the firmly established GGI such as (V, W)C_x, which was rarely dissolved in the Co binder around the WC/Co interfaces, the grain boundary sliding by dislocation climb was significantly hindered during the densification mechanism of the carbide. Therefore, as the WC grains were continuously

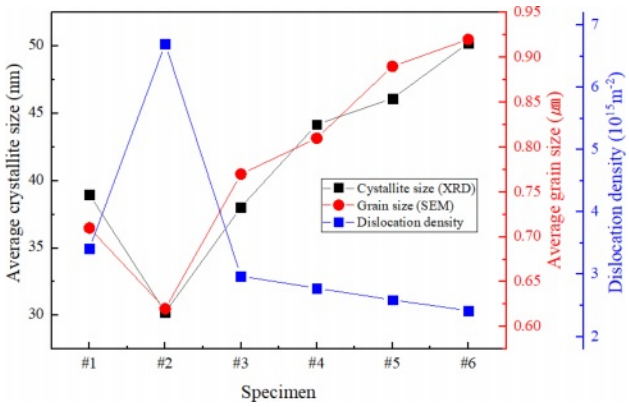

Fig. 4. The variation of average crystallite and grain size, and dislocation density of WC-Co-VC-Cr_3C_2 cermet (#1: WC-6Co, #2: WC-6Co-2.5VC, #3: WC-6Co-2.5VC-0.5Cr_3C_2, #4: WC-6Co-2.5VC-1.0Cr_3C_2, #5: WC-6Co-2.5VC-1.5Cr_3C_2, and #6: WC-6Co-2.0Cr_3C_2).

rearranged during recrystallization, the distance between adjacent grain boundaries decreased, which could lead to a dense and fine-grained interface with a high interfacial energy state [17].

Figure 5 shows the micro-strain due to the lattice parameter variation of the WC-Co-VC-Cr_3C_2 cermet combinations (#1 to #6). Generally, carbides can form non-stoichiometric compounds in a wide composition range depending on the carbon content, forming a solid solution [22]. The stress and strain distributions inside the lattice could be determined according to the carbon content in the solid solution, such as (V, Cr, W)C_x. In the case of #2, it can be seen that the lattice parameter decreased (2.481 → 2.474 Å) as the strain increased (0.32 → 0.61) compared to #1 during the powder densification process. It was believed to act as a solid solution strengthening agent with low carbon content in

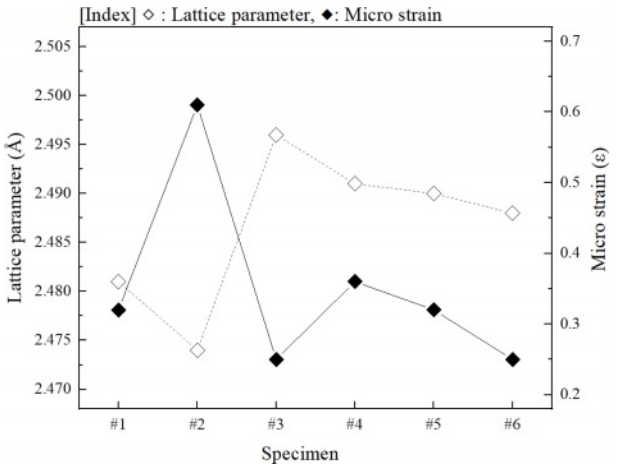

Fig. 5. Evolution of lattice parameter (Å) and micro strain in (35.52~36.20)° range of the WC-Co-VC-Cr_3C_2 cermet (#1: WC-6Co, #2: WC-6Co-2.5VC, #3: WC-6Co-2.5VC-0.5Cr_3C_2, #4: WC-6Co-2.5VC-1.0Cr_3C_2, #5: WC-6Co-2.5VC-1.5Cr_3C_2, and #6: WC-6Co-2.0Cr_3C_2).

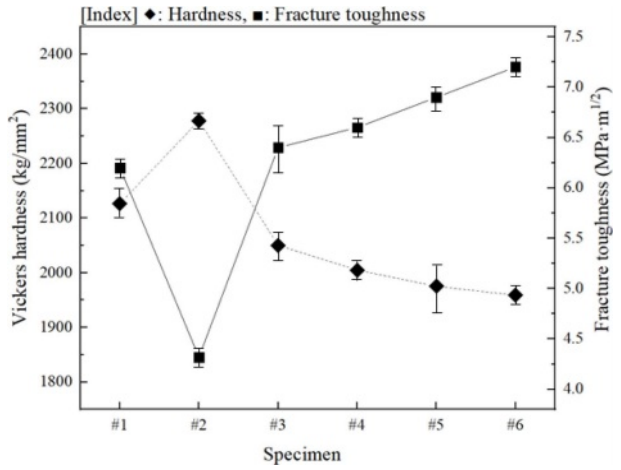

Fig. 6. Mechanical properties of the WC-Co-VC-Cr_3C_2 cermet (#1: WC-6Co, #2: WC-6Co-2.5VC, #3: WC-6Co-2.5VC-0.5Cr_3C_2, #4: WC-6Co-2.5VC-1.0Cr_3C_2, #5: WC-6Co-2.5VC-1.5Cr_3C_2, and #6: WC-6Co-2.0Cr_3C_2).

the lattice distorted by compressive stress. The formation of more (V, W)C_x could lead to a disordered WC_{1-x} interface in a metastable state with a carbon-free orientation owing to compressive stress [17], which may have further enhanced the stability of the interface. However, the co-addition of (V, Cr, W)C_x contributed to an increase in the lattice parameter (2.481 → 2.496 Å) by tensile stress owing to the large amount of Cr dissolved into Co, which caused a high carbon content at the WC/Co interface.

Figure 6 shows the mechanical properties of the WC-Co-VC-Cr_3C_2 cermets (#1 to #6). The hardness increased from #1 to #2 (2126. 4 → 2278.0 kg/mm^2), whereas it rapidly decreased from #3 to #6 (2050.3 → 1958.9 kg/mm^2). In the case of #2, the grain boundary strengthening due to the Hall patch relationship and solid solution strengthening effect due to the high strain were considered to interact and produce the highest hardness value. On the other hand, the fracture toughness value of each WC-Co-VC-Cr_3C_2 cermet (#1 to #6) was determined based on the degree of stress distribution (δ_y) via crack propagation by the applied load indentation. Moreover, the stress intensity magnification factor (K_1) gradually increased, and the material fractured when the stress was concentrated at the tip of the crack. As the distribution distance of the cracks decreased, the K_1 and δ_y values increased. Therefore, high fracture toughness could be expected for the stress distribution over a wide area (*see* Eq. (5)) [23]:

$$\delta_y = \frac{K_1}{(2\pi\gamma)^{1/2}},\ K_1 = s(\pi a)^{1/2}, \tag{5}$$

Where δ_y is the stress distribution at the crack propagation length (r), K_1 is the stress intensity factor, and 2a is the indentation length. The variations in the stress distribution in each cermet are listed in Table 1. Because the stress was applied with the same load (HV_{20}), the "δ_y" value increased as the "r" value decreased. Consequently the #6 cermet showed the highest fracture toughness, *i.e.*, 7.3 MPa ·m$^{1/2}$. This was attributed to the difference in the interfacial energies of the interfacial states established after sintering. For example, in the case of #6, Co was distributed over a wide area, along with coarsened WC grains. For instance, in the fracture behavior of #6, a relatively high fracture toughness was achieved because the tip of the crack was absorbed or deflected [24] into the ductile Co throughout the transgranular fracture, which propagated into the coarsened WC grains.

Conclusion

This study investigated the effects of using VC and Cr_3C_2 in WC-Co cemented carbide. The WC-Co-VC-Cr_3C_2 cermets with different carbides (0.5, 1.0, 1.5, and 2.0 wt% were obtained using SPS. The experimental results are summarized as follows.

1. Densification: The consolidation behavior depended on the comprehensive sintering kinetics, including the densification strain, sintering exponent, macro-shrinkage, and alloy components. The WC-6Co exhibited a high relative density (100.0%), which was close to the theoretical density, because it had the highest densification strain. This corresponded to the lowest sintering exponent due to highly active diffusion routes at the lattice and grain boundaries during the densification

Table 1. Variation of stress distribution and related parameters with sintering temperature of WC-Co-VC-Cr_3C_2 cermet.

Sample	Indentation length (2a)	Average crack length of 4 direction (r)	Stress by applied load stress (s)	Stress intensity factor (K_1)	Stress distribution (σ_y)
WC-6Co (#1)	0.150 mm	0.205 mm	89.16 N/m^2	43.26 MPa·m$^{1/2}$	38.13 N/m^2
WC-6Co-2.5VC (#2)	0.145 mm	0.217 mm		42.54 MPa·m$^{1/2}$	36.44 N/m^2
WC-6Co-2.5VC-0.5Cr_3C_2 (#3)	0.152 mm	0.206 mm		43.55 MPa·m$^{1/2}$	38.29 N/m^2
WC-6Co-2.5VC-1.0Cr_3C_2 (#4)	0.154 mm	0.207 mm		43.84 MPa·m$^{1/2}$	38.45 N/m^2
WC-6Co-2.5VC-1.5Cr_3C_2 (#5)	0.156 mm	0.209 mm		44.12 MPa·m$^{1/2}$	38.51 N/m^2
WC-6Co-2.0Cr_3C_2 (#6)	0.158 mm	0.210 mm		44.40 MPa·m$^{1/2}$	38.66 N/m^2

process.

2. Microstructure: The grain boundary morphology and distribution were determined by the solid solubility of Cr and V in Co during the recrystallization of WC, which also caused AGG to the basal facet, depending on the interface stability and interfacial energy throughout WC/Co. With an increase in the co-addition of VC/Cr_3C_2, the grain size gradually increased from 0.71 to 0.92 μm. In contrast, the single addition of VC caused grain refinement owing to the formation of a firmly established (V, W)Cx complexion at the interface, which had a high dislocation density (6.70×10^{15} m^{-2}) and played a role in hindering intergranular dislocation glide during grain boundary migration.

3. Mechanical behavior: The hardening mechanism of the WC-Co-VC-Cr_3C_2 cermet depended on the grain size, lattice strain, and dislocation density, with the highest hardness value of 2278.0 kg/mm^2 found with the addition of VC owing to the solid solution strengthening. In contrast, the toughening mechanism depended on the stress distribution via crack propagation at the interface, with a value of 7.3 MPa·$m^{1/2}$ obtained with the co-addition of VC (2.5 wt%) and Cr_3C_2 (2.0 wt%).

Acknowledgements

This study has been conducted with the support of the Korea Institute of Industrial Technology (KITECH), “Development of Core Technologies for a Smart Mobility” (KITECH-JA-23-0118).

Conflicts of interest: The authors declare that they have no known competing financial interests or personal relationships that could have appeared to influence the work reported in this paper.

References

1. J. Chen, M. Gong, and S. Wu, J. Ceram. Process. Res. 16 (2015) 244-248.
2. H.S. Yang, J.H Pee, H.T. Kim, and Y.J. Kim, J. Ceram. Process. Res. 13 (2012) 319-323.
3. H.K. Park, H.J. Youn, S.M. Lee, H.S. Bang, and I.H. Oh, J. Ceram. Process. Res. 12 (2011) 304-309.
4. K.M. Fox, J.R. Hellmann, H. Izuia, M.F. Amateaub, W. Fuc, and P.H. Cohenc, J. Ceram. Process. Res. 5 (2004) 18-24.
5. J.H. Lee, I.H. Oh, and H.K. Park, Arch. Metall. Mater. 66 (2021) 1029-1032.
6. H.K. Park, I.H. Oh, J.H. Kim, S.K. Hong, and J.H. Lee, Arch. Metall. Mater. 66 (2021) 997-1000.
7. H.C.A. Chee, R.S.K. Singh, and K.Y.S Lee, J. Ceram. Process. Res. 21 (2020) 495-500.
8. Y.K. Sun, D.Y. Li, P. Gao, Z. Lu, and H. Ge, J. Ceram. Process. Res. 17 (2016) 499-503.
9. J.H. Lee and H.K. Park, J. Ceram. Process. Res. 22 (2021) 655-664.
10. J.H. Lee and H.K. Park, J. Ceram. Process. Res. 22 (2021) 590-596.
11. A.A.M. El-Almir, S. Li, M. Abdelgawad, and E.M.M. Ewais, J. Korean Ceram. Soc. 58 (2021) 574-582.
12. R. Chen, S. Zheng, R. Zhou, B. Wei, G. Yang, P. Chen, and J. Cheng, Int. J. Refract. Met. Hard Mater. 103 (2022) 105751.
13. T. Lin, Q. Li, Y. Han, K. Song, X. Wang, H. Shao, J. Dong, H. Wang, and X. Deng, Int. J. Refract. Met. Hard Mater. 103 (2022) 105782.
14. M. Basak, L. Rahman, Md. F. Ahmed, B. Biswas, and N. Sharmin, J Alloys Compd. 895 (2022) 162694.
15. S. Pramanik, A.K. Srivastav, B.M. Jolly, N. Chawake, and B.S. Murty, Adv. Powder Technol. 30 (2019) 2779-2786.
16. T.A. Fabijanic, D. Coric, M.S. Musa, and M. Sakoman, Metals 7 (2017) 143.
17. J.H. Lee, S.K. Hong, and H.K. Park, Int. J. Refract. Met. Hard Mater. 100 (2021) 105649.
18. K. Mannesson, I. Borgh, A. Borgenstam, and J. Ågren, Int. J. Refract. Met. Hard Mater. 29 (2011) 488-494.
19. A.Y. Fong, Y. Kodera, M. Murata, T. Imai, H. Xu, M.R. Dirmyer, S.J. Obrey, and J.E. Garay, Mater. Sci. Eng. B 259 (2020) 114607.
20. X. Liu, X. Song, H. Wang, X. Liu, F. Tang, and H. Lu, Acta Mater. 149 (2018) 164-178.
21. Y.B. Peng, Y. Du, P. Zhou, W.B. Zhang, W.M. Chen, L. Chen, S.Q. Wang, and G.H. Xie, Int. Refract. Met. Hard Mater. 42 (2014) 57-70.
22. J. Garcia, V.C. Cipres, A. Blomqvist, and B. Kaplan, Int. Refract. Met. Hard Mater. 80 (2019) 40-68.
23. Y.F. Meng, Y.B. Zhu, L.C. Zhou, X.S. Meng, Y.L. Yang, R. Zhao, J. Xia, B. Yang, Y.J. Lu, H.A. Wu, L.B. Mao, and S.H. Yu, Adv. Mater. 34 (2022) 2108267.
24. R. Kerans and T.A. Parthasarathy, Compos. Part A Appl. Sci. 30 (1999) 521-524.